Nucleation and transformation of Zr-bearing dispersoids in Al-Mg-Si 6xxx alloys

Ali Elasheri [a], Emad M. Elgallad [a,*], Nick Parson [b], X.-Grant Chen [a,*]

[a] Department of Applied Science, University of Quebec at Chicoutimi, Saguenay (QC), Canada G7H 2B1

[b] Arvida Research and Development Centre, Rio Tinto Aluminium, Saguenay (QC), Canada G7S 4K8

(*Corresponding author: Emad_Elgallad@uqac.ca and xgrant_chen@uqac.ca)

Abstract

The nucleation and transformation of $L1_2$-Al_3Zr and DO_{22}-$(Al,Si)_3Zr$ dispersoids in Al-Mg-Si 6xxx alloys were studied using interrupted quenching and transmission electron microscopy. Spherical $L1_2$-Al_3Zr dispersoids precipitated preferentially along $\langle 001 \rangle_{Al}$ in early stages of nucleation, coinciding with the same sites and orientation of β' precipitates that dissolved during heating. Two nucleation mechanisms were suggested to explain this preferable precipitation. At a relatively low heat treatment temperature (400 °C), the $L1_2$-Al_3Zr dispersoids were predominant, and no transformation occurred. With further increase in temperature to 550 °C, the $L1_2$-Al_3Zr dispersoids started to transform into DO_{22}-$(Al,Si)_3Zr$. At high temperatures, elongated DO_{22}-$(Al,Si)_3Zr$ dispersoids, which were formed through the transformation of pre-existing $L1_2$ dispersoids rather than the direct precipitation from the supersaturated aluminum solid solution, became the dominant phase.

Keywords: Al-Mg-Si 6xxx alloys, Zr-bearing dispersoids, nucleation, transformation

Taxonomy selected keywords: Al; Mg; nucleation & growth; phase transformation; Si; Zr

Introduction

Microalloying Zr in aluminum alloys is widely used to control the grain structure, improve recrystallization resistance, and enhance mechanical properties and corrosion resistance [1-5]. Such effects are achieved via the precipitation of nano-sized Zr-bearing dispersoids. Owing to the low solubility of Zr in α-Al, Zr supersaturation in the solid solution can be obtained during solidification, providing the driving force for the precipitation of Zr-bearing dispersoids during the subsequent heat treatment. Zr exhibits extremely low diffusivity in the aluminum matrix, thereby improving the thermal stability and coarsening resistance of the formed dispersoids [6, 7]. However, the precipitation behavior of such dispersoids can be affected by other alloying elements and heat treatment parameters.

The decomposition of the supersaturated solid solution during heat treatment results in the initial formation of nanoscale $L1_2$-Al_3Zr dispersoids [8]. However, the nucleation of $L1_2$-Al_3Zr dispersoids is considerably affected by the local supersaturation level. For instance, high precipitation rates are observed in the interiors of dendrite cells/grains owing to the large Zr concentration as a result of Zr segregation during solidification [9]. By contrast, a significantly lower concentration of Zr is found in the interdendritic regions, resulting in weaker precipitation [10]. In addition, other alloying elements can affect the nucleation of Zr-bearing dispersoids. For instance, Cu and Zn reportedly accelerate the precipitation of Al_3Zr via $CuAl_2$ in Al-Cu-Zr alloys [11, 12], and $MgZn_2$ precipitates in Al-Mg-Zr alloys [11, 12], acting as nucleation sites. Si significantly promotes the precipitation of Zr-bearing dispersoids through Si-vacancy clusters that act as heterogeneous sites for such dispersoids [13]. Moreover, Si improves the diffusion kinetics of Zr in the aluminum matrix, thus reducing the peak-aging time of Zr-bearing dispersoids [14].

Zr-bearing dispersoids can exist in different crystal structures depending on the heat treatment condition. At relatively low temperatures (300 °C to 450 °C), high-symmetry cubic $L1_2$-Al_3Zr dispersoids with spherical morphology and small size commonly precipitate. Such type of dispersoids exhibits a coherent interface with the matrix owing to their good mismatch with the aluminum matrix [15]. This metastable $L1_2$-Al_3Zr can eventually transform to tetragonal structure phases (DO_{22} or DO_{23}) at high temperatures (exceeding 500 °C) [6, 16]. Although the incoherent DO_{23} with elongated morphology is the most stable phase that typically exists at high temperatures, the semi-coherent DO_{22} precipitates instead of DO_{23} when the alloy contains a considerable amount of Si [17]. It has been reported that Si stabilizes DO_{22} by promoting the phase transformation from $L1_2$ to DO_{22}. This transformation occurs by substituting Al with a small amount of Si and changing the structure of $L1_2$ to DO_{22} instead of the stable DO_{23}. The stability of $L1_2$ is affected by the addition of Si through decreasing the stacking fault energy of $L1_2$, which subsequently lowers the barrier for the transformation to DO_{22} [18].

Our previous work [19] reported that Al-Mg-Si 6xxx alloys with various Si levels contained two types of Zr-bearing dispersoids, namely $L1_2$ and DO_{22} dispersoids, which can affect the deformed grain structure and recrystallization resistance. However, the precipitation behavior of these dispersoids, including their nucleation and transformation during homogenization, has not been well understood yet. Through the use of Zr-containing 6xxx model alloys, this work aims to investigate the precipitation behavior of Zr-bearing dispersoids during heat treatment, particularly their nucleation and transformation mechanisms. Alloy samples were subjected to interrupted quenching in water at different temperatures and times during heat treatment (homogenization) process. The evolution of the dispersoids was subsequently investigated using transmission electron microscopy (TEM) to better understand their nucleation and transformation.

Results and discussion

The nucleation of $L1_2$ dispersoids

Figure 1 shows the bright-field TEM images of the H-Si alloy samples quenched at 200 °C, 300 °C, and 400 °C during the heating ramp from ambient temperature to 400 °C. The H-Si alloy contains 0.99 wt.% Si and a Mg/Si ratio of ~1. When the samples were heated to 200 °C, numerous fine needle-shaped MgSi precipitates with dimensions of 5 ± 0.8 nm in diameter and 35 ± 8 nm in length (Fig. 1a) appeared along $<001>_{Al}$. The small black dots (arrowed) are the cross-sections of these precipitates. The corresponding selected area diffraction pattern (SADP, see the inset in Fig. 1a) showed cross-shaped streaks along $<001>_{Al}$ directions. Based on their morphology, size and SADP, the fine precipitates in Fig. 1a were identified to be the coherent β''-Mg_5Si_6 precipitates [20-22]. Increasing the temperature to 300 °C resulted in coarsening of the precipitates, which reached 10 ± 3.5 nm in width and 400 ± 77 nm in length (Fig. 1b) with faint reflections in the corresponding SADP (see the inset in Fig. 1b) due to their precipitation on $\{200\}_{Al}$ planes, suggesting the transformation to β'-$Mg_{1.8}Si$ precipitates [23-25]. When the sample temperature reached 400 °C, the number density of β' precipitates was significantly reduced and few equilibrium β-Mg_2Si particles were observed (Fig. 1c) showing their diffraction spots in the relevant SADP [25, 26], implying the dissolution and transformation of the metastable β' precipitates. Evidently, the supersaturated solid solution enriched with Mg and Si after solidification was decomposed during heating to form metastable MgSi precipitates [24]. Meanwhile, the TEM observations did not reveal any Zr-bearing dispersoids at this stage.

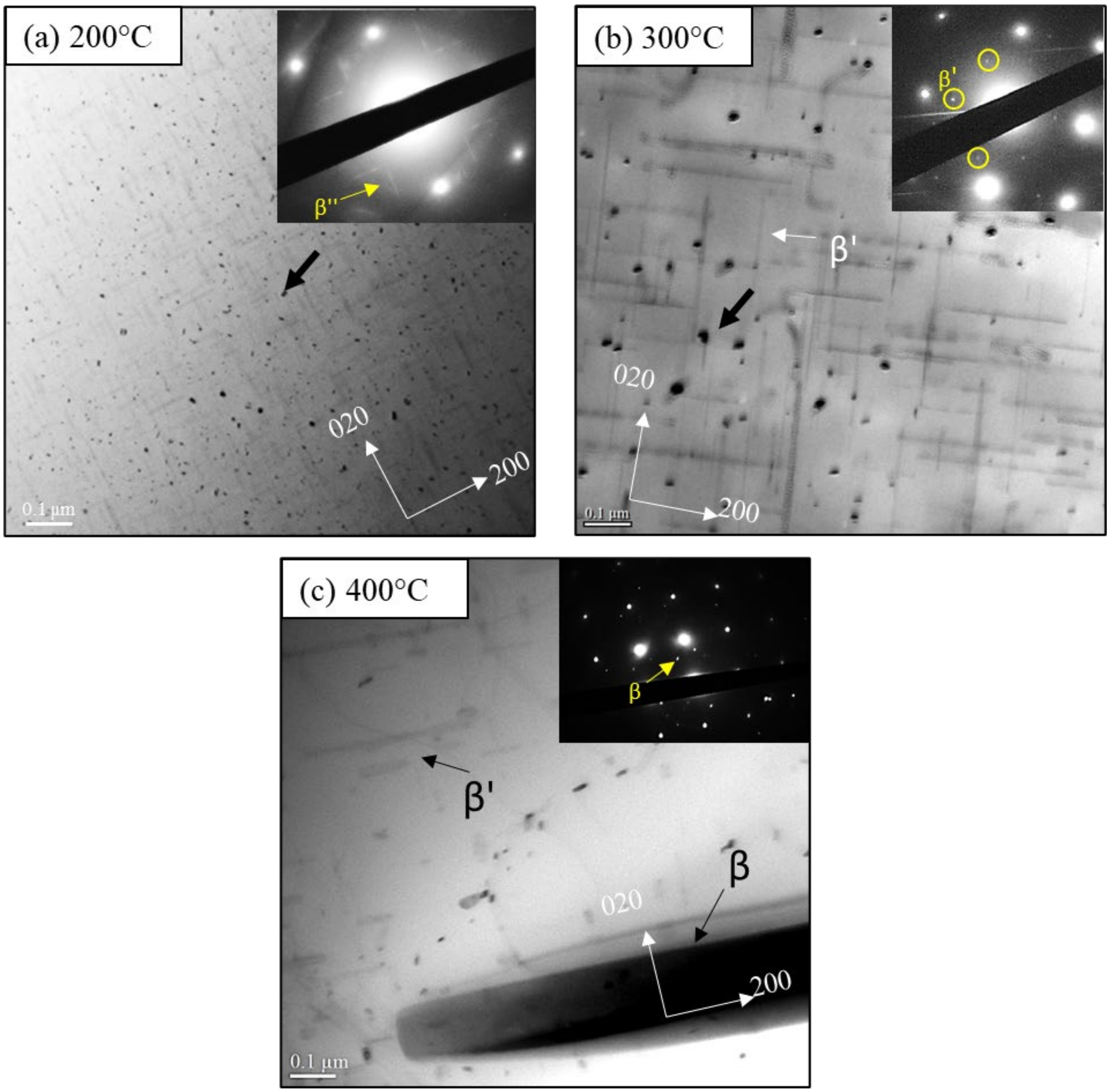

Figure 1 Bright-field TEM images showing the precipitation of β'' and β' in the H-Si alloy during heating ramp to 400 °C quenched at (a) 200 °C, (b) 300 °C, and (c) 400 °C.

When the samples were isothermally held at 400 °C, fine dispersoids with spherical morphology were precipitated. Figure 2a-d shows the dark-field TEM images of the dispersoids after holding at 400°C for different durations. After 2 h, a few tiny dispersoids (few nm) were observed as shown in Fig. 2a. Based on their spherical morphology and the corresponding SADP (Fig. 2e), these dispersoids were identified as $L1_2$-Al_3Zr dispersoids [27]. Further isothermal holding at 400 °C for 5 h resulted in a significant increase in the number density of $L1_2$-Al_3Zr dispersoids (Fig. 2b). Interestingly, these dispersoids exhibited a preferred orientation along $<001>_{Al}$, which was the same orientation as that of the previous β'-$Mg_{1.8}Si$ precipitates (Fig. 1b). With further holding to 12 h, a considerably increased number of Al_3Zr dispersoids precipitated and grew, as shown in Fig. 2c. The preferred precipitation direction of the dispersoids along $<001>_{Al}$ was still observed, indicating that the majority of Al_3Zr dispersoids nucleated and grew on the previous β'-$Mg_{1.8}Si$ sites. In addition, the nucleation of $L1_2$ dispersoids and β' precipitates on the same $\{100\}_{Al}$ habit plane is evidenced by comparing the corresponding diffraction patterns in Fig. 2e and f, respectively. As the isothermal holding was prolonged to 48 h, the preferred orientation became less apparent owing to the precipitation of numerous dispersoids (Fig. 2d), which would be explained hereafter.

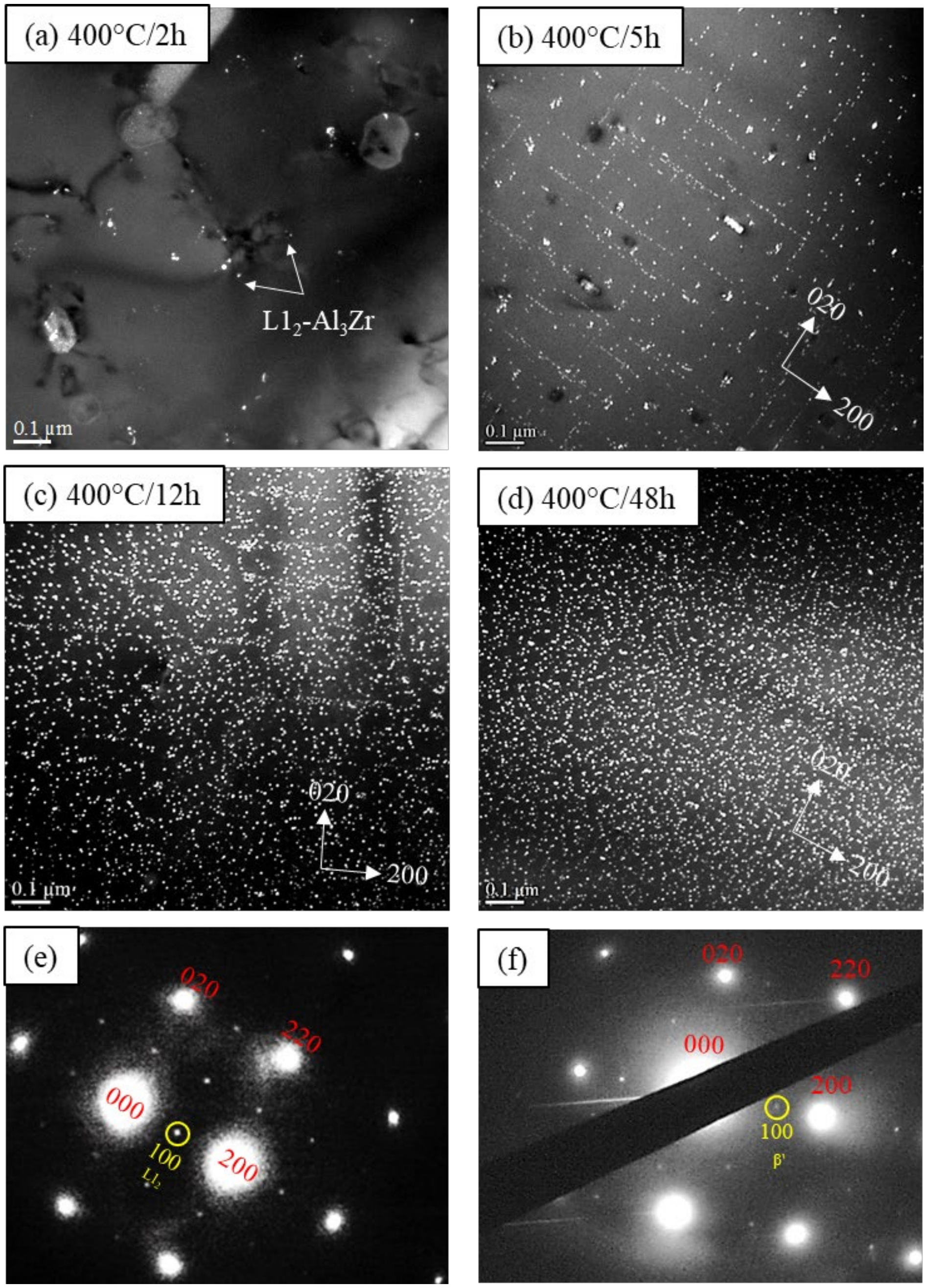

Figure 2 Dark-field TEM images of H-Si samples isothermally held at 400 °C for (a) 2 h, (b) 5 h, (c) 12 h, and (d) 48 h at 400 °C, showing the precipitation of L1$_2$-Al$_3$Zr dispersoids and diffraction patterns of (e) L1$_2$-Al$_3$Zr and (f) β'-Mg$_{1.8}$Si.

Figure 3 shows a bright-field TEM image of the L-Si alloy quenched at 300 °C and dark-field TEM images after isothermal holding at 400 °C for 5 and 48 h. The L-Si alloy contained 0.39 wt.%

Si and a Mg/Si ratio of ~1. Compared with the H-Si alloy (Figs. 1 and 2), the L-Si alloy exhibited markedly less precipitation of both MgSi precipitates and Al_3Zr dispersoids. The low Mg and Si levels in the L-Si alloy resulted in a less supersaturated solid solution, which consequently reduced the amount of β'-$Mg_{1.8}Si$ precipitates as shown in Fig. 3a. Similar to the H-Si alloy, spherical $L1_2$-Al_3Zr dispersoids were preferentially precipitated along <001>$_{Al}$ after holding for 5 and 48 h at 400 °C, which was the same preferred orientation of the previous β' precipitates. The lower number density of $L1_2$-Al_3Zr dispersoids in the L-Si alloy relative to that of the H-Si alloy (Fig. 3b and c vs. Fig. 2b and d) appeared to be proportional to the number density of the β' precipitates.

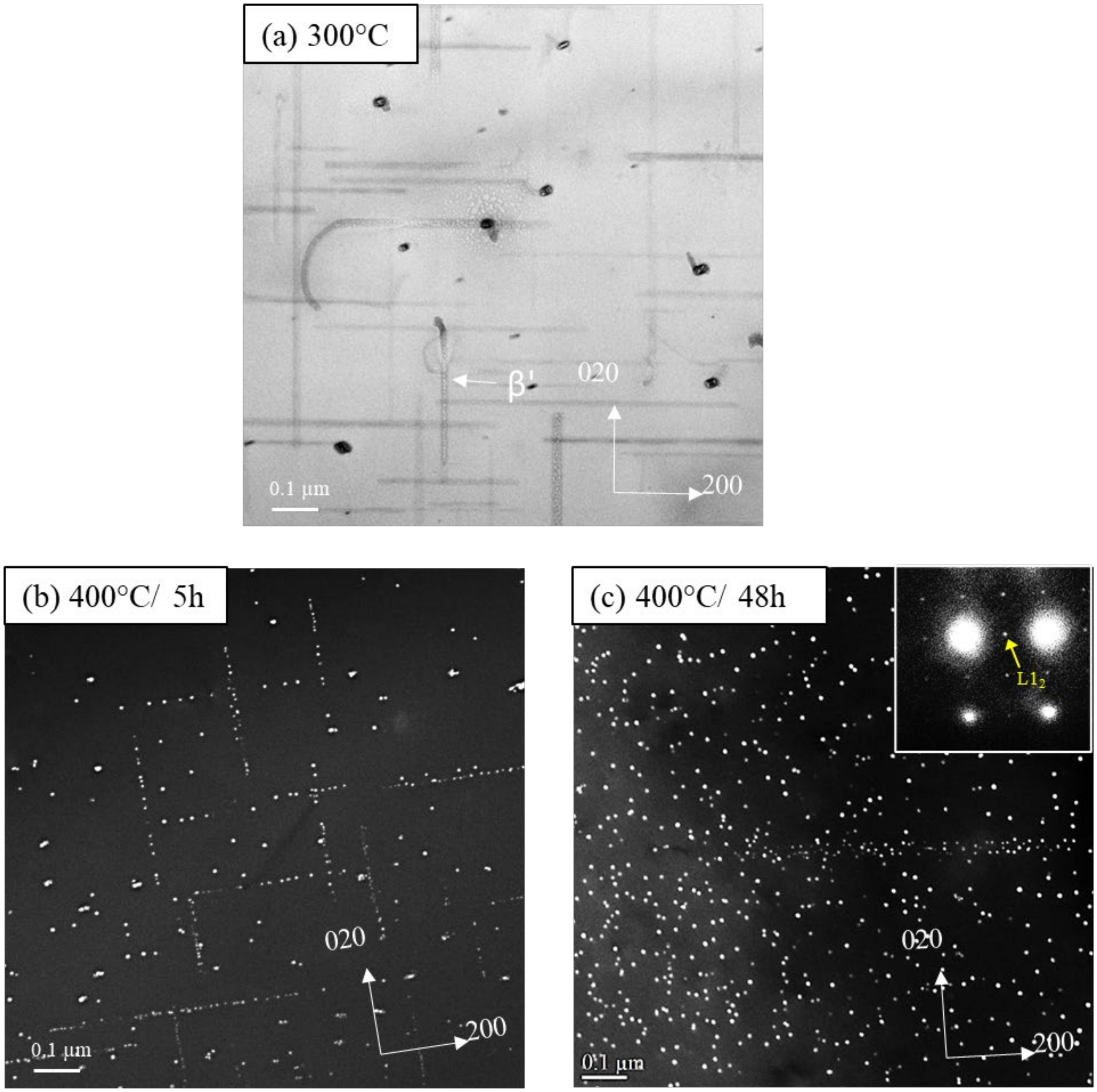

Figure 3 a) Bright-field TEM image showing the precipitation of β'-$Mg_{1.8}Si$ in the L-Si alloy quenched at 300 °C and the dark-field TEM images of $L1_2$-Al_3Zr precipitation after isothermal holding at 400 °C for (b) 5 h and (c) 48 h.

The above results suggest that the pre-existing β'-$Mg_{1.8}Si$ precipitates that form and subsequently dissolve during heating ramp to the precipitation temperature of the $L1_2$-Al_3Zr dispersoids (~400 °C) provide favorable nucleation sites of $L1_2$-Al_3Zr in both L-Si and H-Si alloys.

These sites become enriched by Si atoms after the dissolution of β'-$Mg_{1.8}Si$ precipitates. Zhen *et al*. [28] observed higher Si concentration at the sites of dissolved β'- $Mg_{1.8}Si$ precipitates compared to that in the surrounding aluminum matrix, resulting in local Si-enriched sites. In the present study, such sites promoted the nucleation of Al_3Zr dispersoids during isothermal holding. Owing to the strong attractive energy between Si and vacancies, Si-vacancy clusters can form and serve as nucleation sites for Al_3Zr dispersoids as previously reported [13, 29, 30]. Several studies reported the significant effect of Si on the precipitation kinetics of trialuminides in general and that of Al_3Zr in particular [14, 29, 31]. Another possible scenario for the favorable precipitation of $L1_2$-Al_3Zr dispersoids at the sites of the dissolved β'-$Mg_{1.8}Si$ precipitates is that Zr atoms might be dragged by the Al/β' interfaces as observed in several studies in the case of θ'-Al_2Cu precipitates [32-34]. As a result, the high concentration of Zr atoms at these interfaces provides the driving force for the precipitation of $L1_2$-Al_3Zr at the sites of the dissolved β' precipitates. Notably, precipitation of $L1_2$ dispersoids was not observed on the equilibrium β-Mg_2Si particles when these dispersoids started to precipitate.

The precipitation of $L1_2$-Al_3Zr dispersoids can also vary with the supersaturation of Zr solutes across the dendrite grain. The level of Zr supersaturation plays an essential role that affects the activation energy barrier for nucleation and, consequently, the amount of precipitation [9]. Zr atoms are enriched in the centers of dendrite cells/grains owing to their segregation during solidification [35]. Figure 4 displays a montage of dark-field TEM images (assembly of several images) showing the precipitation of Al_3Zr dispersoids in the H-Si alloy from the grain boundary toward the grain interior after holding at 400 °C for 12 h. On the left-hand side, few $L1_2$ dispersoids appeared because of the low Zr supersaturation level near the grain boundaries, taking into consideration that the partition coefficient of Zr in Al is greater than unity (k ~2.5), which enriched the Zr in the dendrite centers at the expense of grain boundary areas. The preferred precipitation direction of $L1_2$ dispersoids along <001> $_{Al}$ was evident, coinciding entirely with the orientation of the previous β' precipitates. Moving toward the grain center, Zr supersaturation increased: consequently, the number density of Al_3Zr dispersoids increased, reaching a maximum in the grain center (right-hand side). The preferred orientation along <001> $_{Al}$ became less visible compared to that of the region close to the grain boundary.

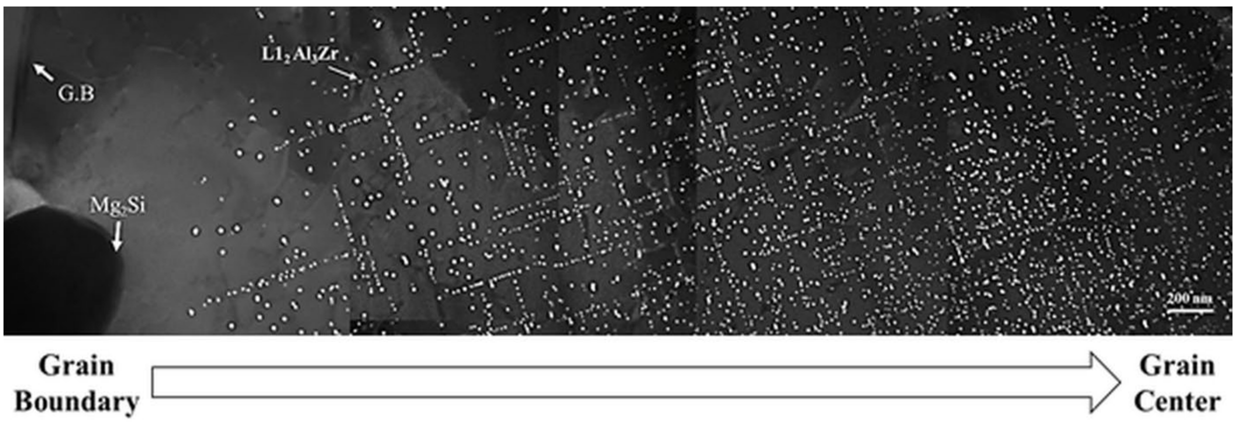

Figure 4 Montage of dark-field TEM micrographs of the H-Si alloy after holding at 400 °C for 12 h, showing the precipitation of Al_3Zr dispersoids across the grain.

The Transformation of $L1_2$ to DO_{22}

The transformation of $L1_2$ to DO_{22} dispersoids was often observed during homogenization or heat treatment at high temperatures [19, 36]. Thus, the H-Si alloy was selected to study the transformation behavior of the Zr-bearing dispersoids attributed to the higher number density of dispersoids compared to that of L-Si alloy. Figure 5 shows the TEM images of the dispersoid evolution in the Hi-Si alloy during the heating ramp from 400 °C to 500 °C–550 °C after holding at 400 °C for 48 h (heat treatment II in Fig. 1). Compared with the large quantity of $L1_2$-Al_3Zr dispersoids observed at 400 °C for 48 h (Fig. 2d), the number density of relatively large $L1_2$

dispersoids was significantly reduced after ramping to 500 °C (Fig. 5a). Meanwhile, some dispersoids with an elongated morphology and large size appeared among the fine spherical $L1_2$ dispersoids (circled in Fig. 5b). Notably, no elongated dispersoids were observed during holding at 400 °C for 48 h, indicating that such dispersoids were developed during heating to 500 °C. When the temperature was increased to 550 °C, the quantity of $L1_2$ dispersoids was further reduced (Fig. 5c), while more elongated large dispersoids appeared in the aluminum matrix (Fig. 5d). These elongated dispersoids were identified as the DO_{22}-$(Al,Si)_3Zr$ phase by TEM with energy-dispersive X-ray spectroscopy (EDS) and the corresponding SADP [36]. The DO_{22}-$(Al,Si)_3Zr$ dispersoid possesses a tetragonal crystal structure and is mainly precipitated at high temperatures in 6xxx alloys [17, 37, 38]. The coarse DO_{22} dispersoids also appeared to align along $<001>_{Al}$, suggesting that their appearance was closely related to the pre-existing $L1_2$ dispersoids (Fig. 5d).

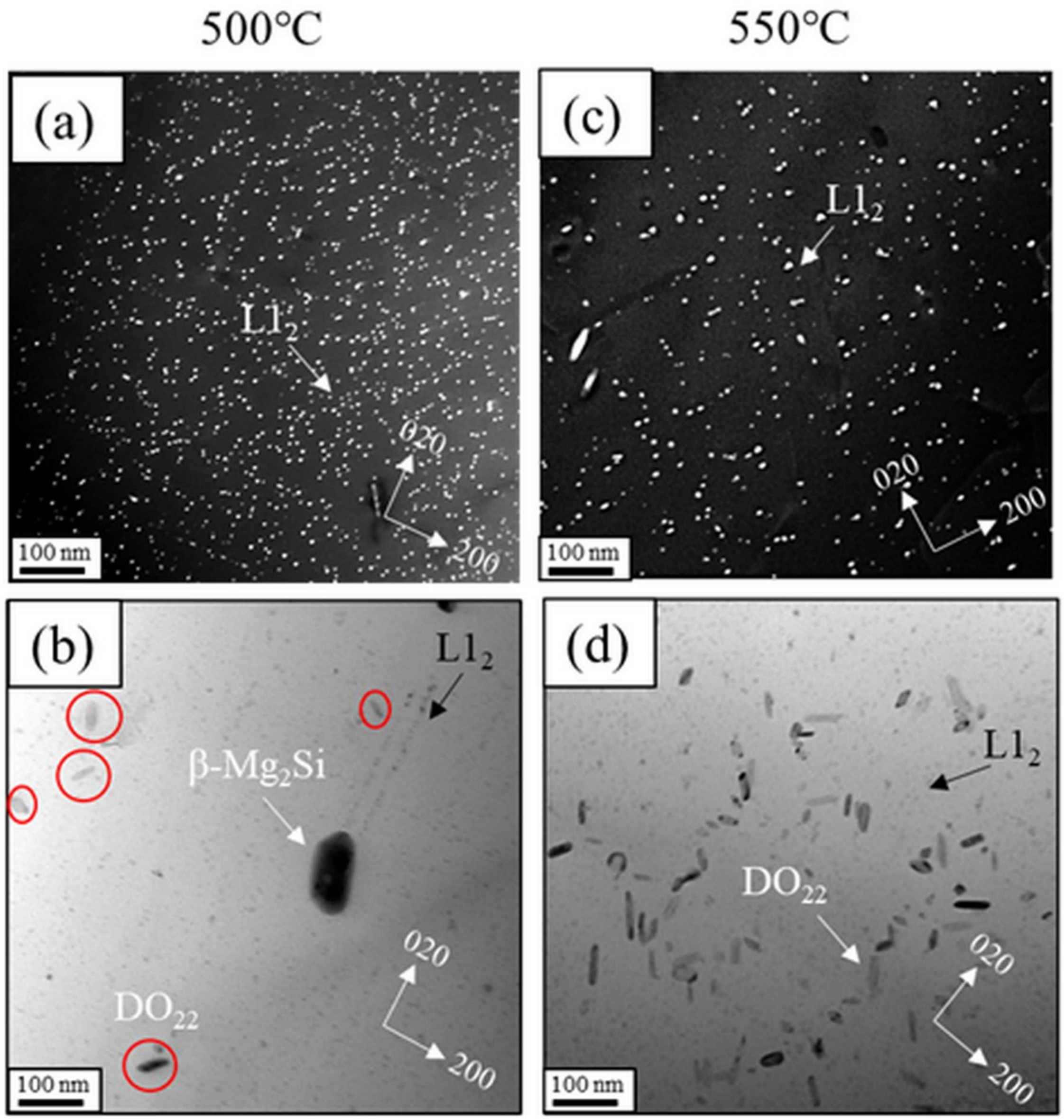

Figure 5 The evolution of Zr-bearing dispersoids after holding at 400 °C for 48 h and subsequent heating to (a,b) 500 °C and (c,d) 550 °C.

Figure 6 shows bright-field TEM images of the dispersoid transformation from spherical Ll$_2$ dispersoids into elongated DO$_{22}$ dispersoids, as well as the TEM-EDS line scans of Si and Zr distribution. The samples were heated from 400 °C to 550 °C after holding at 400 °C for 48 h. First, the spherical L1$_2$ dispersoids coarsened (Fig. 6a) via the Ostwald ripening mechanism by the dissolution of surrounding smaller $L1_2$ dispersoids [2]. At this stage, the distribution of Si through the particle showed a negligible change relative to that in the matrix. Subsequently, the spherical $L1_2$ dispersoids developed an ellipsoidal morphology (Fig. 6b) with a slight but notable increase in Si and a considerable increase in Zr, indicating that a transition stage between the spherical $L1_2$ and the elongated DO_{22} dispersoids occurred. Eventually, the dispersoids enlarged considerably and transformed to elongated DO_{22} particles (Fig. 6c) driven by the diffusion of additional Si into the particle, as evidenced by the large peak of Si count in the TEM-EDS line scan. Si decreases the stacking fault energy in $L1_2$ dispersoids and consequently lowers the energy barrier for the transformation of metastable $L1_2$ dispersoids to stable DO_{22} dispersoids [18].

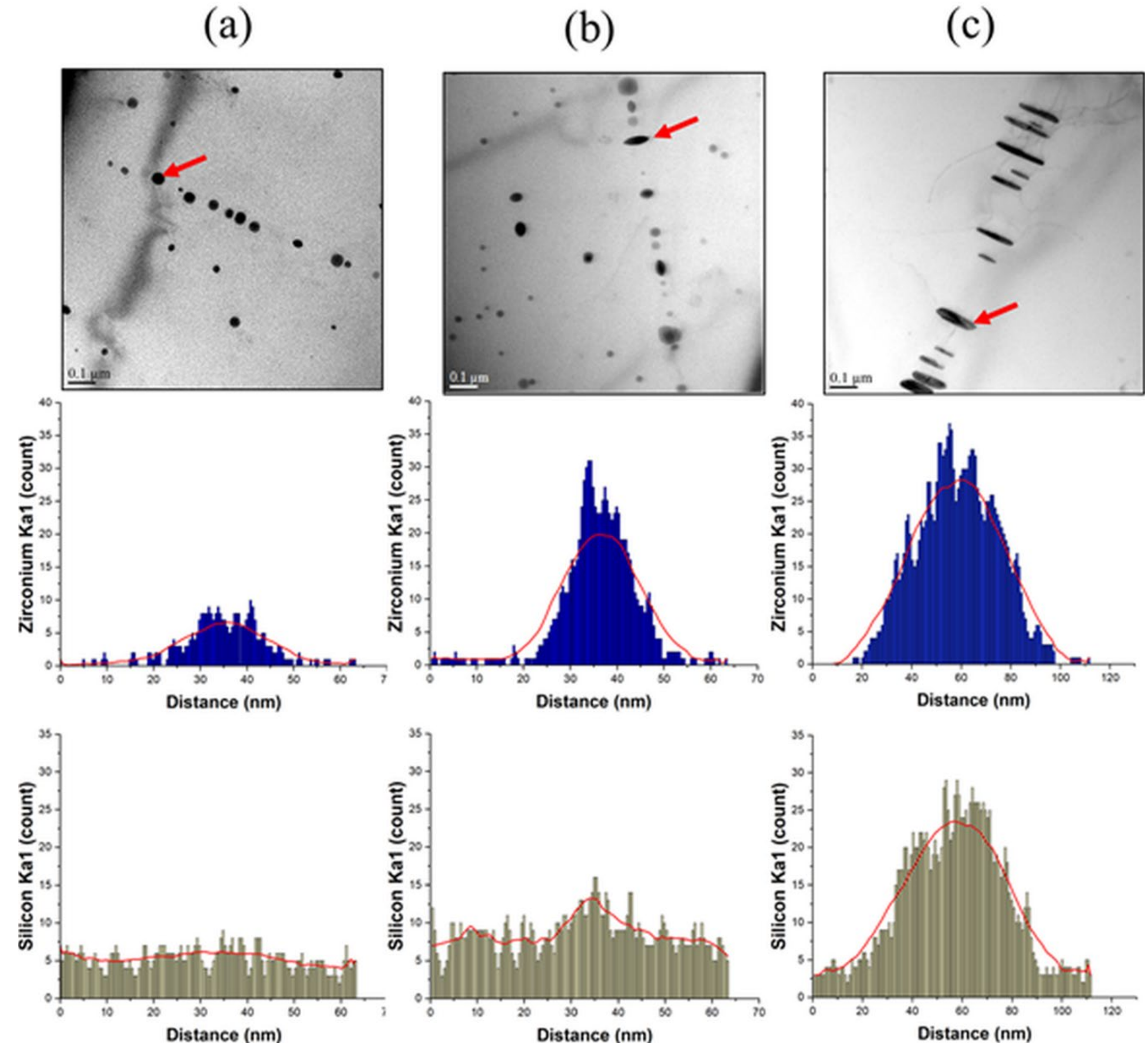

Figure 6 Bright-field TEM images showing the transformation process of Zr-bearing dispersoids after holding at 400 °C for 48 h and then heating to 550 °C, and the corresponding TEM-EDS line scans of Si and Zr distribution across typical dispersoids (arrowed): (a) spherical, (b) ellipsoidal, and (c) elongated dispersoids.

A thorough TEM examination revealed the details of the transformation sequence from spherical L1$_2$ dispersoids to elongated DO$_{22}$ dispersoids, as shown in Fig. 7. Structural faults developed inside the coarse spherical dispersoids (Fig. 7a). These faults were characterized by sharp lines of dark contrast parallel to <001>$_{Al}$ in the middle of the dispersoids. Similar faults that were attributed to the anti-phase boundary (APB) generated by the transition to an imperfect tetragonal DO_{23} were reported by other studies [39]. Therefore, these faults represent the early stages of the transformation of $L1_2$ to the DO_{22} structure. Subsequently, several APBs developed in the particles exhibited preferential growth along <001>$_{Al}$, resulting in an ellipsoidal morphology with a long axis along the anti-phase boundaries, as shown in Fig. 7b and its insert. Eventually, the coarsening and growth of the ellipsoidal dispersoids resulted in a complete transformation to elongated DO_{22} dispersoids (Fig. 7c). With multiplying APBs in the particle and further growth, the preferential growth direction of the elongated dispersoids could deviate from the <001>$_{Al}$, as shown in Figs. 5(d) and 7(c).

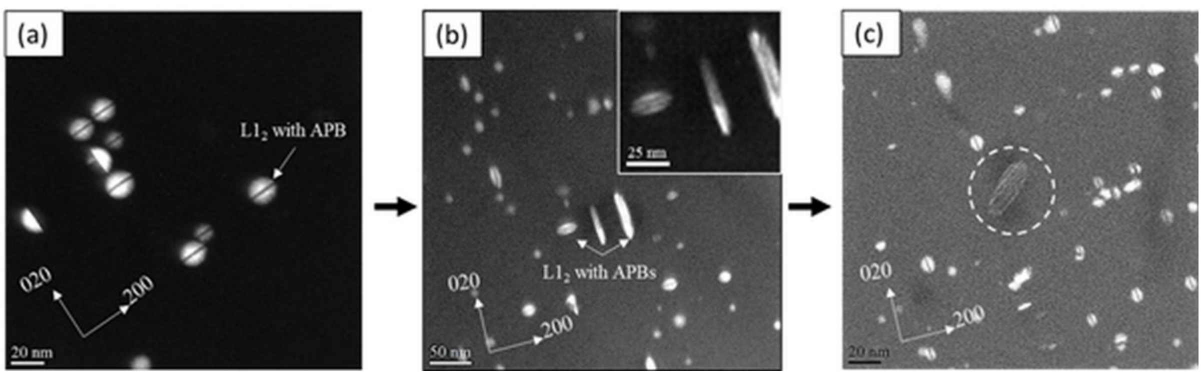

Figure 7 Dark-field TEM images showing the transformation sequence of spherical $L1_2$ to elongated DO_{22} dispersoids: (a) developing the anti-phase boundary (APB) in $L1_2$ particles, (b) growth with an ellipsoidal morphology and several APBs, and (c) transforming to elongated DO_{22} particles with multiplying APBs.

Precipitation of dispersoids during one-step treatment

Figure 8 shows the precipitation of both $L1_2$ and DO_{22} dispersoids after ramp heating directly from room temperature to 500 °C–550 °C with and without holding for 5 h (heat treatment III, one-step heat treatment in Fig. 10). The dark-field TEM images were inserted in each corresponding bright-field TEM image to better show the $L1_2$ dispersoids. During heating to 500

°C (Fig. 8a), nanosized $L1_2$-Al_3Zr dispersoids (indicated by white arrows) precipitated mainly along <001> $_{Al}$. In addition, a limited quantity of small DO_{22} dispersoids (indicated by black arrows) was observed. After holding at 500 °C for 5 h (Fig. 8b), $L1_2$ dispersoids underwent coarsening (white arrow), resulting in a significant reduction of the number density, while some DO_{22} dispersoids grew (black arrow). At this intermediate temperature, $L1_2$ and DO_{22} dispersoids co-existed. Meanwhile, the increase in temperature from 500 °C to 550 °C (Fig. 8c) also resulted in a reduction of $L1_2$ dispersoids, accompanied by their transformation to the elongated DO_{22} dispersoids, which exhibited the same orientation as the pre-existing $L1_2$ dispersoids. A dispersoid-free zone around the aligned $D0_{22}$ dispersoids was observed, suggesting the dissolution of surrounding $L1_2$ particles during the transformation and growth of $D0_{22}$ dispersoids. Subsequently, the transformed DO_{22} dispersoids coarsened after holding at 550 °C for 5 h (Fig. 8d), accompanied by the complete dissolution of the spherical $L1_2$-Al_3Zr dispersoids. The DO_{22} dispersoids were mostly transformed from pre-existing $L1_2$-type dispersoids rather than nucleated directly from the supersaturated aluminum solid solution; this mechanism was demonstrated by the alignment of DO_{22} dispersoids along <001> $_{Al}$, which coincided with the orientation of the $L1_2$ dispersoids formed earlier. In addition, the coarsening of the DO_{22} dispersoids occurred by the dissolution of the nearby pre-existing $L1_2$ dispersoids, which were less thermodynamically stable at elevated temperatures than DO_{22}.

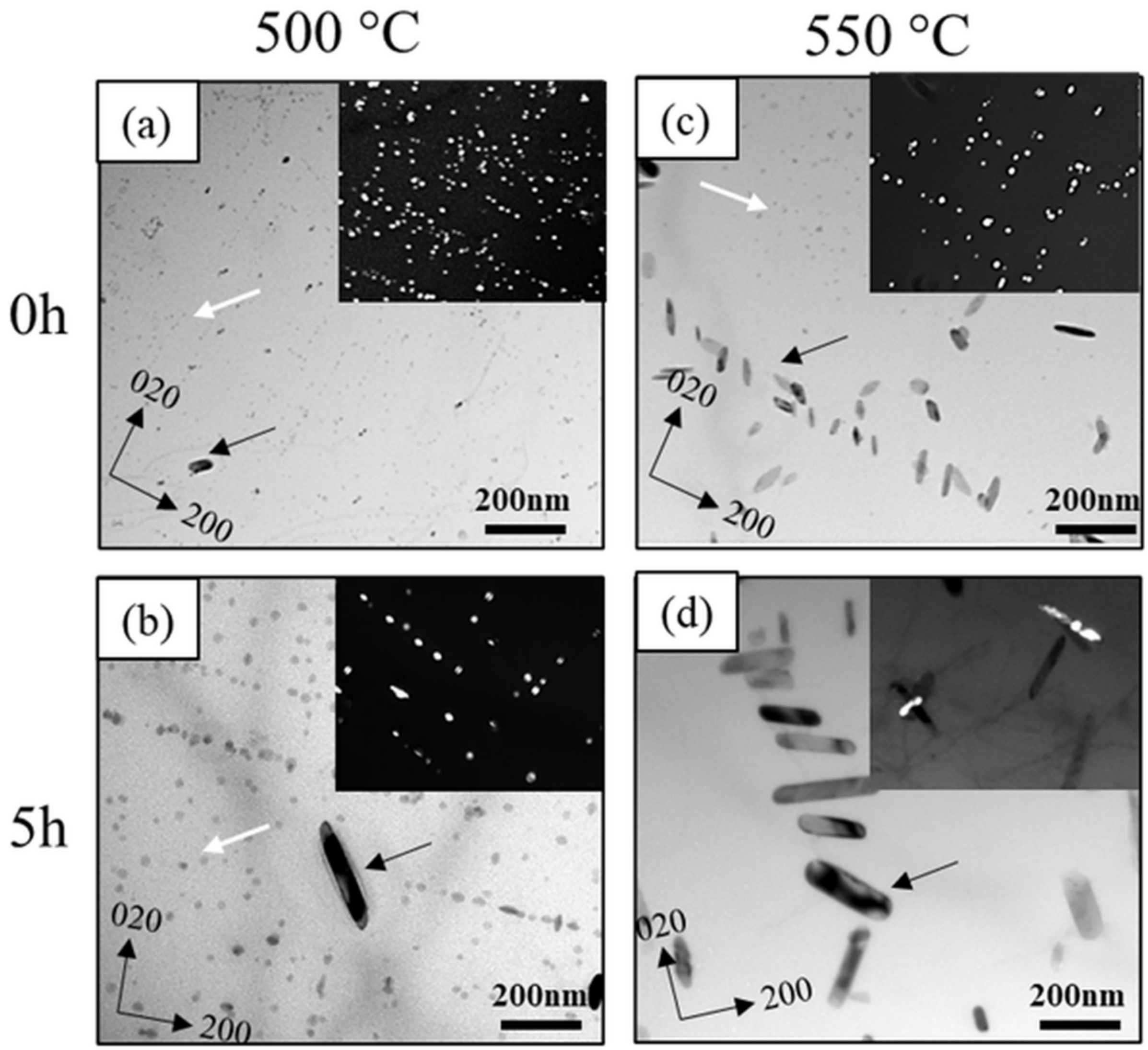

Figure 8 The evolution of Zr-bearing dispersoids after direct heating from room temperature to (a) 500 °C and (c) 550 °C, and after holding (b) at 500 °C for 5 h and (d) at 550 °C for 5 h.

Figure 9 presents a schematic illustration of the nucleation and transformation mechanisms for Zr-bearing dispersoids during heat treatment for both L-Si and H-Si alloys. In the early stage of the heating ramp (200 °C), a large number of tiny metastable β'' precipitates formed with a needle-shaped morphology. Two possible mechanisms may control the nucleation of $L1_2$-Al_3Zr dispersoids with increasing the temperature. In the first mechanism, the β'' precipitates grew and transformed to β' precipitates with a lath-like morphology (Fig. 9a.1) which subsequently dissolved leaving Si-enriched sites (Fig. 9b.1). This promotes the formation of Si-vacancy clusters, which provides favorable nucleation sites for $L1_2$-Al_3Zr dispersoids after holding at 400 °C (Fig. 9c). Alternatively, the other mechanism suggests that Zr atoms might be dragged by Al/β' interfaces at 300 °C (Fig. 9a.2). With increasing the temperature to 400 ºC, the β' precipitates dissolved leaving areas with high concentrations of Zr atoms (Fig. 9b.2), which provides a favorable nucleation condition for the precipitation of $L1_2$-Al_3Zr in these areas during holding at 400 °C (Fig. 9c).

With further extension of the holding time at 400 °C, more Al_3Zr dispersoids precipitated and grew, resulting in a random distribution of dispersoids (Fig. 9d). At a relatively low heat treatment temperature, the $L1_2$-Al_3Zr dispersoids predominated in the aluminum matrix, and no transformation of dispersoids occurred. When the temperature was increased to 550 °C, the $L1_2$ dispersoids became unstable and started to coarsen via the Ostwald ripening mechanism, while the coarse dispersoids began to transform to the elongated DO_{22}-$(Al,Si)_3Zr$ that exhibited the same orientation as the pre-existing $L1_2$ dispersoids (Fig. 9e). Finally, with increased holding time at a high temperature, all of the remaining $L1_2$ dispersoids completely transformed to DO_{22} dispersoids (Fig. 9f). Evidently, DO_{22} dispersoids were mostly transformed from pre-existing $L1_2$-type dispersoids rather than precipitated directly from the aluminum matrix.

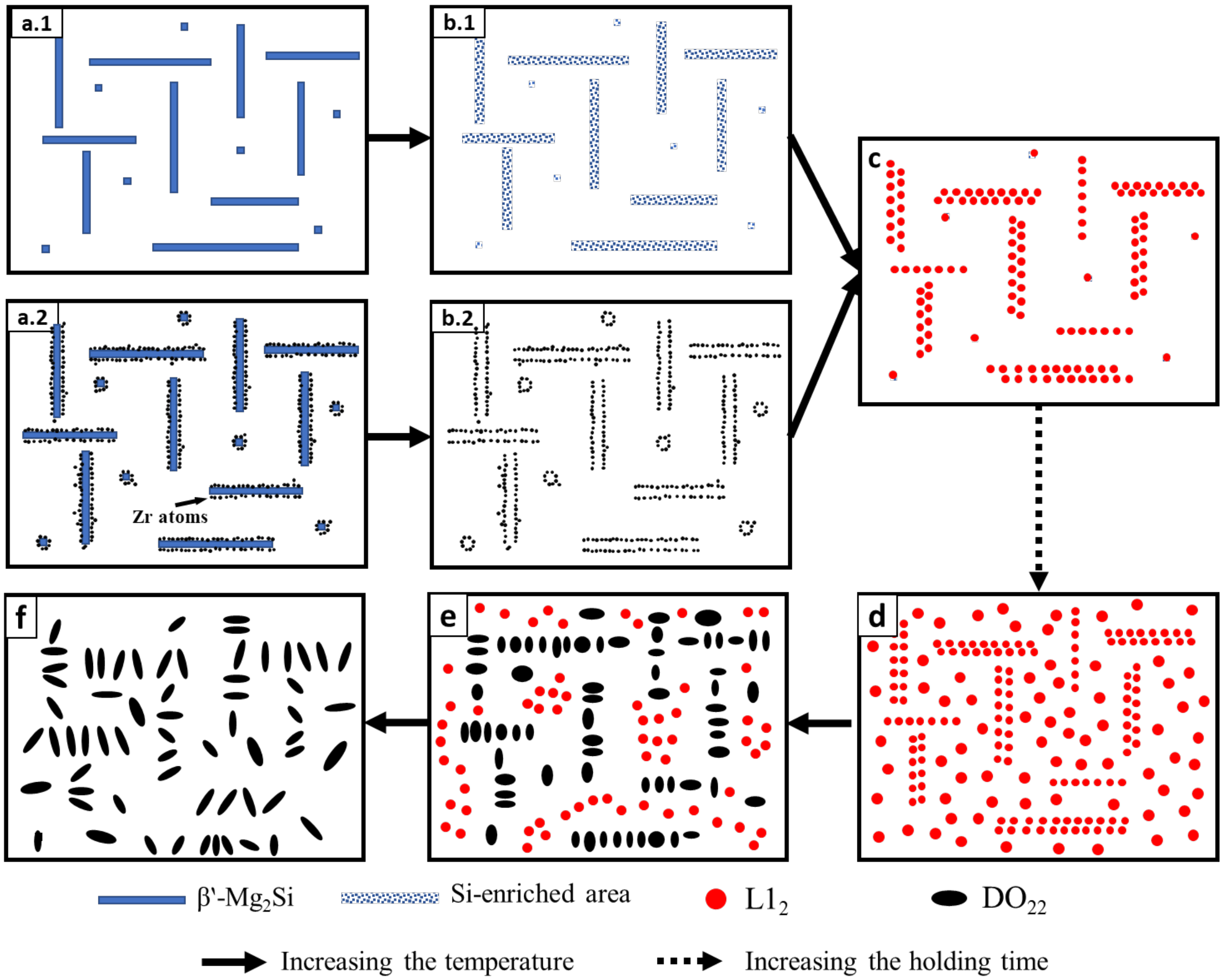

Figure 9 Schematic illustration of the nucleation and transformation of Zr-bearing dispersoids in Al-Mg-Si 6xxx alloys.

Conclusions

(1) At the early stages of nucleation at 400 °C, spherical L1$_2$-Al$_3$Zr dispersoids were precipitated along $\langle 001 \rangle_{Al}$, coinciding with the orientation of β'-Mg$_{1.8}$Si phase that precipitated and subsequently dissolved during heating. Two nucleation mechanisms were proposed to explain the preferable precipitation of L1$_2$-Al$_3$Zr dispersoids at the sites of the dissolved β' precipitates.

(2) With prolonging of the holding time at 400 °C, a significant increase in the number density of $L1_2$ dispersoids was observed. At this relatively low heat treatment temperature, the spherical $L1_2$-Al_3Zr dispersoids predominated in the aluminum matrix, and no transformation occurred.

(3) With increasing heat treatment temperature, spherical $L1_2$-Al_3Zr dispersoids started to transform to elongated DO_{22}-$(Al,Si)_3Zr$. The transformation of $L1_2$ dispersoids was initiated by the introduction and multiplication of anti-phase boundaries. Preferential growth along $\langle 001 \rangle_{Al}$ initially resulted small ellipsoidal dispersoids that gradually grew, attaining complete transformation to elongated DO_{22} dispersoids.

(4) At a high temperature (~550 °C), the elongated DO_{22}-$(Al,Si)_3Zr$ dispersoids, which were formed by the transformation of pre-existing $L1_2$ dispersoids rather than by direct precipitation from the supersaturated solid solution, were the dominant Zr-bearing phase in the microstructure.

Experimental procedure

Two Al-Mg-Si 6xxx model alloys containing 0.15 % Zr and with two levels of Si and Mg, designated as H-Si and L-Si alloys, were used in this study. The H-Si contains 0.99% Si, 0.89% Mg, 0.18% Fe and 0.14% Ti, while the L-Si alloy has 0.39% Si, 0.35% Mg, 0.16% Fe and 0.13% Ti (all alloy compositions are given in wt.%, analyzed by the optical emission spectrometer). The Mg/Si atomic ratio in both alloys was designed to be close to 1, which is preferred in Al-Mg-Si extrusion alloys to promote artificial aging response. The alloys were prepared using pure Al (99.7%) and Mg (99.8%) as well as Al-50% Si, Al-25% Fe, Al-5% Ti-1% B and Al-15% Zr master alloys. The materials were melted in an electrical resistance furnace and cast into a permanent steel mould preheated to 250 °C to obtain rectangular cast ingots with dimensions of 30 × 40 × 80 mm. Samples from cast ingots were subjected to different heat treatment (homogenization) procedures involving the interrupted quench in water to room temperature at different temperatures and times, as shown in Fig. 10. Regarding the nucleation of $L1_2$-Al_3Zr dispersoids, a series of samples were heated from room temperature to 400 °C at a low heating rate of 50 °C/h and isothermally held for different times. This relatively low temperature was chosen to promote the sole precipitation of $L1_2$-Al_3Zr dispersoids (heat treatment I). As a second step (after 400 °C for 48 h), some of these samples were further heated up to 550 °C at a high heating rate of 150 °C/h to study the stability/transformation of the pre-existing $L1_2$-Al_3Zr dispersoids (heat treatment II). The high heating rate was used to minimize the possible further precipitation of $L1_2$-Al_3Zr dispersoids during heating. In addition, some samples were directly heated from room temperature to 500 °C and 550 °C at a high heating rate of 150°C/h (heat treatment III) for comparison with heat treatment II.

A transmission electron microscopy (TEM, JEM-2100) equipped with an energy-dispersive X-ray spectroscopy (EDS) operated at 200 kV was used to observe the Zr-bearing dispersoids. The quenched samples were first mechanically ground to approximately 40–60 μm, and then electropolished using a twin-jet electropolisher operated at 15 V and -20 °C with 30 vol.% nitric acid and 70 vol.% methanol. The dark-field mode of TEM was primarily used for the observation of Ll_2-Al_3Zr dispersoids using $L1_2$ superlattice reflection of precipitates along <001> zone axis. For DO_{22}-$(Al,Si)_3Zr$ dispersoid observation, the bright-field mode of TEM near <001> zone axis of the aluminum matrix was used.

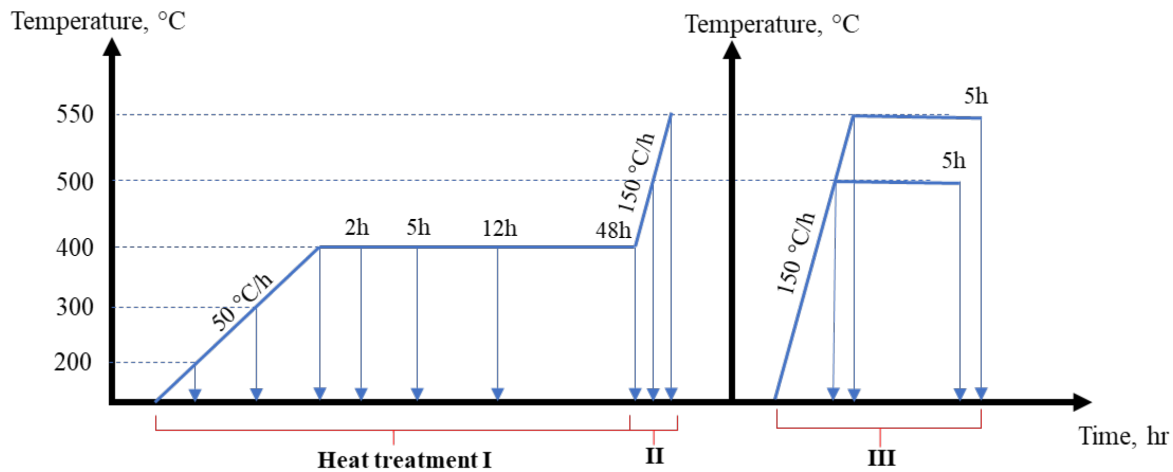

Figure 10 Different heat treatment procedures and interrupted water quench.

Acknowledgments

The authors would like to acknowledge the financial support of the Natural Sciences and Engineering Research Council of Canada (NSERC) and Rio Tinto Aluminum under the Grant No. CRDPJ 514651-17 through the Research Chair in the Metallurgy of Aluminum Transformation at University of Quebec at Chicoutimi.

Declarations

Funding

The financial support was provided by Natural Sciences and Engineering Research Council of Canada (NSERC) and Rio Tinto Aluminum under the Grant No. CRDPJ 514651-17.

Conflicts of interest

The authors declare no conflict of interest.

Availability of data and material

Supporting data could be available upon reasonable request.

Code availability

Not applicable

Authors' contributions

A. Elasheri: Methodology, Investigation, Formal Analysis, Writing-Original Draft; E.M. Elgallad: Methodology, Validation, Writing-Review and Editing; N. Parson: Methodology, Resources, Writing-Review and Editing; X.-G. Chen: Methodology, Validation, Writing-Review and Editing; Project Administration.

References

1. K. Chen, H.-C. Fang, Z. Zhang, X. Chen and G. Liu, Effect of of Yb, Cr and Zr additions on recrystallization and corrosion resistance of Al–Zn–Mg–Cu alloys. *Mater. Sci. Eng., A.* **497**(1-2), 426 (2008).
2. Y. Li, B. Lu, W. Yu, J. Fu, G. Xu and Z. Wang, Two-stage homogenization of Al-Zn-Mg-Cu-Zr alloy processed by twin-roll casting to improve L12 Al3Zr precipitation, recrystallization resistance, and performance. *J. Alloys Compd.* **882**, 160789 (2021).
3. M.-X. Zhang, C. Wang, S.-Y. Zhang, X. Liu, X. Wang, M.-W. Ren and H.-Y. Wang, Enhanced aging precipitation behavior and mechanical properties of 6022 Al–Mg–Si alloy with Zr addition. *Mater. Sci. Eng., A.* **840**, 142957 (2022).
4. S. Griffiths, J.R. Croteau, M.D. Rossell, R. Erni, A. De Luca, N.Q. Vo, D.C. Dunand and C. Leinenbach, Coarsening- and creep resistance of precipitation-strengthened Al–Mg–Zr alloys processed by selective laser melting. *Acta Mater.* **188**, 192 (2020).
5. L. Zhou, H. Hyer, J. Chang, A. Mehta, T. Huynh, Y. Yang and Y. Sohn, Microstructure, mechanical performance, and corrosion behavior of additively manufactured aluminum alloy 5083 with 0.7 and 1.0 wt% Zr addition. *Mater. Sci. Eng., A.* **823**, 141679 (2021).
6. E. Clouet, J.M. Sanchez and C. Sigli, First-principles study of the solubility of Zr in Al. *Phys. Rev. B.* **65**(9), 094105 (2002).
7. H. Li, J. Bin, J. Liu, Z. Gao and X. Lu, Precipitation evolution and coarsening resistance at 400°C of Al microalloyed with Zr and Er. *Scripta Mater.* **67**(1), 73 (2012).
8. E. Nes, Precipitation of the metastable cubic Al3Zr-phase in subperitectic Al-Zr alloys. *Acta Metall.* **20**(4), 499 (1972).

9. J.D. Robson and P.B. Prangnell, Dispersoid precipitation and process modelling in zirconium containing commercial aluminium alloys. *Acta Mater.* **49**(4), 599 (2001).

10. Q. Liu, G. Fan, Z. Tan, Z. Li, D. Zhang, J. Wang and H. Zhang, Precipitation of Al3Zr by two-step homogenization and its effect on the recrystallization and mechanical property in 2195 Al–Cu–Li alloys. *Mater. Sci. Eng., A.* **821**, 141637 (2021).

11. Z.-H. Jia, J.-P. Couzinié, N. Cherdoudi, I. Guillot, L. Arnberg, P. Åsholt, S. Brusethaug, B. Barlas and D. Massinon, Precipitation behaviour of Al3Zr precipitate in Al–Cu–Zr and Al–Cu–Zr–Ti–V alloys. *Trans. Nonferrous Met. Soc. China.* **22**(8), 1860 (2012).

12. A.V. Mikhaylovskaya, A.G. Mochugovskiy, V.S. Levchenko, N.Y. Tabachkova, W. Mufalo and V.K. Portnoy, Precipitation behavior of L12 Al3Zr phase in Al-Mg-Zr alloy. *Mater. Charact.* **139**, 30 (2018).

13. S.H. Wu, H. Xue, C. Yang, P.M. Cheng, P. Zhang, J. Kuang, J.Y. Zhang, G. Liu and J. Sun, Effect of Si addition on the precipitation and mechanical/electrical properties of dilute Al–Zr-Sc alloys. *Mater. Sci. Eng., A.* **812**, 141150 (2021).

14. N.Q. Vo, D.C. Dunand and D.N. Seidman, Role of silicon in the precipitation kinetics of dilute Al-Sc-Er-Zr alloys. *Mater. Sci. Eng., A.* **677**, 485 (2016).

15. T.-A. Pan, Y.-C. Tzeng, H.-Y. Bor, K.-H. Liu and S.-L. Lee, Effects of the coherency of Al3Zr on the microstructures and quench sensitivity of Al–Zn–Mg–Cu alloys. *Mater. Today Commun.* **28**, 102611 (2021).

16. K.E. Knipling, D.C. Dunand and D.N. Seidman, Criteria for developing castable, creep-resistant aluminum-based alloys–A review. *Zeitschrift für Metallkunde.* **97**(3), 246 (2006).

17. L. Litynska, D. Abou-Ras, G. Kostorz and J. Dutkiewicz, TEM and HREM study of Al3Zr precipitates in an Al-Mg-Si-Zr alloy. *J Microsc.* **223**(Pt 3), 182 (2006).

18. F. Schmid, D. Gehringer, T. Kremmer, L. Cattini, P.J. Uggowitzer, D. Holec and S. Pogatscher, Stabilization of Al3Zr allotropes in dilute aluminum alloys via the addition of ternary elements. *Acta Mater.* **21**, 101321 (2022).

19. A. Elasheri, E.M. Elgallad, N. Parson and X.G. Chen, Evolution of Zr-Bearing Dispersoids during Homogenization and Their Effects on Hot Deformation and Recrystallization Resistance in Al-0.8%Mg-1.0%Si Alloy. *J. Mater. Eng. Perform.* **30**(10), 7851 (2021).

20. S.J. Andersen, H.W. Zandbergen, J. Jansen, C. TrÆholt, U. Tundal and O. Reiso, The crystal structure of the β″ phase in Al–Mg–Si alloys. *Acta Mater.* **46**(9), 3283 (1998).

21. W. Yang, M. Wang, R. Zhang, Q. Zhang and X. Sheng, The diffraction patterns from β ″precipitates in 12 orientations in Al–Mg–Si alloy. *Scripta Mater.* **62**(9), 705 (2010).

22. R.S. Yassar, D.P. Field and H. Weiland, Transmission electron microscopy and differential scanning calorimetry studies on the precipitation sequence in an Al–Mg–Si alloy: AA6022. *J. Mater. Res.* **20**(10), 2705 (2005).

23. R. Vissers, M.v. van Huis, J. Jansen, H. Zandbergen, C. Marioara and S. Andersen, The crystal structure of the β′ phase in Al–Mg–Si alloys. *Acta Mater.* **55**(11), 3815 (2007).

24. G.A. Edwards, K. Stiller, G.L. Dunlop and M.J. Couper, The precipitation sequence in Al–Mg–Si alloys. *Acta Mater.* **46**(11), 3893 (1998).

25. M.J. Starink and A.M. Zahra, β′ and β precipitation in an Al–Mg alloy studied by DSC and TEM. *Acta Mater.* **46**(10), 3381 (1998).

26. Y. Ohmori, L.C. Doan, Y. Matsuura, S. Kobayashi and K. Nakai, Morphology and crystallography of β-Mg2Si precipitation in Al-Mg-Si alloys. *Materials Transactions.* **42**(12), 2576 (2001).

27. N. Belov, T. Akopyan, N. Korotkova, M. Murashkin, V. Timofeev and A. Fortuna, Structure and Properties of Ca and Zr Containing Heat Resistant Wire Aluminum Alloy Manufactured by Electromagnetic Casting. *Metals.* **11**(2), 236 (2021).

28. Z. Li, Z. Zhang and X.G. Chen, Effect of Metastable Mg2Si and Dislocations on α-Al(MnFe)Si Dispersoid Formation in Al-Mn-Mg 3xxx Alloys. *Metallurgical and Materials Transactions A.* **49**(11), 5799 (2018).

29. C. Booth-Morrison, Z. Mao, M. Diaz, D.C. Dunand, C. Wolverton and D.N. Seidman, Role of silicon in accelerating the nucleation of Al3(Sc,Zr) precipitates in dilute Al–Sc–Zr alloys. *Acta Mater.* **60**(12), 4740 (2012).

30. T. Sato, A. Kamio and G.W. Lorimer, Effects of Si and Ti Additions on the Nucleation and Phase Stability of the L12-Type Al3Zr Phase in Al-Zr Alloys. *Mater. Sci. Forum.* **217-222**, 895 (1996).

31. N.Q. Vo, D.C. Dunand and D.N. Seidman, Improving aging and creep resistance in a dilute Al–Sc alloy by microalloying with Si, Zr and Er. *Acta Mater.* **63**, 73 (2014).

32. P. Shower, J. Morris, D. Shin, B. Radhakrishnan, J. Poplawsky and A. Shyam, Mechanisms for stabilizing θ′(Al2Cu) precipitates at elevated temperatures investigated with phase field modeling. *Acta Mater.* **6**, 100335 (2019).

33. L. Jiang, B. Rouxel, T. Langan and T. Dorin, Coupled segregation mechanisms of Sc, Zr and Mn at θ′ interfaces enhances the strength and thermal stability of Al-Cu alloys. *Acta Mater.* **206**, 116634 (2021).

34. J.D. Poplawsky, B.K. Milligan, L.F. Allard, D. Shin, P. Shower, M.F. Chisholm and A. Shyam, The synergistic role of Mn and Zr/Ti in producing θ′/L12 co-precipitates in Al-Cu alloys. *Acta Mater.* **194**, 577 (2020).

35. Z. Jia, G. Hu, B. Forbord and J.K. Solberg, Effect of homogenization and alloying elements on recrystallization resistance of Al–Zr–Mn alloys. *Mater. Sci. Eng., A.* **444**(1-2), 284 (2007).

36. A. Elasheri, E.M. Elgallad, N. Parson and X.G. Chen, Effect of Si Level on the Evolution of Zr-Bearing Dispersoids and the Related Hot Deformation and Recrystallization Behaviors in Al–Si–Mg 6xxx Alloys. *Adv. Eng. Mater.*, 2101606 (2022).

37. F. Kahrıman and M. Zeren, Microstructural and Mechanical Characterization of Al-0.80Mg-0.85Si-0.3Zr Alloy. *Archives of Foundry Engineering.* **17**, 73 (2017).

38. Y. Meng, J. Cui, Z. Zhao and L. He, Effect of Zr on microstructures and mechanical properties of an AlMgSiCuCr alloy prepared by low frequency electromagnetic casting. *Mater. Charact.* **92**, 138 (2014).

39. L. Ding, M. Zhao, Z. Jia, Y. Weng, K. Xiang, X. Wu and Q. Liu, On the formation of anti-phase boundaries and interphase boundaries in Al3Zr precipitates of Al-Cu-Zr alloy studied at atomic scale. *J. Alloys Compd.* **887**, 161442 (2021).